

This is the accepted manuscript made available via CHORUS. The article has been published as:

Theoretical uncertainty of (α, n) reactions relevant for the nucleosynthesis of light r-process nuclei in neutrino-driven winds

J. Pereira and F. Montes

Phys. Rev. C **93**, 034611 — Published 15 March 2016

DOI: [10.1103/PhysRevC.93.034611](https://doi.org/10.1103/PhysRevC.93.034611)

Theoretical uncertainty of (α, n) reactions relevant for the nucleosynthesis of light r-process nuclei in neutrino-driven winds

J. Pereira^{1,2} and F. Montes^{1,2}

¹*National Superconducting Cyclotron Laboratory, Michigan State University, East Lansing, MI 48824, USA*

²*Joint Institute for Nuclear Astrophysics, <http://www.jinaweb.org>*

(Dated: January 6, 2016)

Background: Neutrino-driven winds following core-collapse supernova explosions have been proposed as a possible site where *light* r-process nuclei (between Fe and Ag) might be synthesized. In these events, (α, n) reactions are key to move matter towards the region of higher proton number. Abundance network calculations are very sensitive to the rates for this type of reactions.

Purpose: The present work aims at evaluating the theoretical uncertainty of these (α, n) reactions calculated with reaction codes based on the Hauser-Feshbach model.

Method: We compared several (α, n) rates taken from TALYS and the NON-SMOKER database to determine the uncertainties due to the existing technical differences between both codes. In addition, we evaluated the sensitivity of TALYS rates to variations in the alpha optical potentials, masses, level densities, optical potentials, pre-equilibrium intranuclear transition rates, level structure, radiative transmission coefficients, and width-fluctuation correction factors.

Results: The main source of uncertainty at low temperatures are mostly due to the use of different alpha optical potentials. Differences between TALYS and NON-SMOKER at high temperatures arise from the energy binning algorithm used by each code. We have also noticed that the (α, n) rates from the NON-SMOKER database correspond to the inclusive reaction, instead of the exclusive $(\alpha, 1n)$ channel calculated in the present work and used in network calculations.

Conclusions: Theoretical uncertainties in calculated reaction rates can be as high as 1-to-2 orders of magnitude, and strongly dependent on the temperature of the environment. Besides direct measurements of the inclusive and exclusive $(\alpha, 1n)$ reaction rates, experimental studies of alpha optical potentials are crucial to improve the performance of reaction codes.

PACS numbers: 26.30.-k, 26.30.Hj, 26.50.+x, 97.60.Bw

I. INTRODUCTION

Nuclear reactions play a crucial role in the evolution of stars. They are critical to understand the connection between the star “ashes”, constituted by the nuclei generated during the life and death (in some cases violent) of the star, and the underlying nucleosynthesis processes. From a theoretical point of view, nuclear reaction rates depend on the temperature of the environment and several fundamental properties of the nuclei involved, such as masses, level densities, and optical potentials. In the case of steady stellar burning cycles, the ruling reactions involve nuclei near and at the valley of stability, whose properties are well known experimentally. On the other hand, the extreme conditions present in some violent scenarios lead to the synthesis of exotic nuclei which are hard to access experimentally. In those cases, one needs to use reaction codes such as e.g. TALYS [1], NON-SMOKER [2], or CIGAR [3] to calculate the corresponding reaction rates.

The theoretical quest to explain the synthesis of heavy elements has not yet been fully solved. These nuclei are considered to be mainly produced in neutron-capture processes, particularly the s and r processes [4], with other minor contributors like e.g. the p process [5], ν process [6], νp process [7], i process [8], and α process [9]. Advances in this field have been possible through the development of sophisticated astrophysical simulations

aimed at reproducing the large amount of abundance data from observations of metal-poor stars (MPS) (see e.g. [10, 11]). These studies combine hydrodynamical simulations and reaction network calculations. The later are sensitive to both, the astrophysical conditions (e.g. temperature, neutron density, electron fraction), and the properties of the nuclei involved, particularly their reaction rates. In the last years, there have been numerous studies on the role of neutron-capture rates in the nucleosynthesis of heavy elements. These studies focused on understanding the sources of uncertainty of the calculated rates [12, 13], and evaluating the impact of these uncertainties in network-calculated abundances [14–17]. On the contrary, equivalent studies on charge-particle reactions are scarce [9, 18, 19], even though they are known to play a crucial role in the synthesis of *light* r-process nuclei (from Fe to Ag) through the α (or charge-particle) process (see e.g. [9, 20, 21]).

The present work is the first of a series of papers aimed at studying the impact of α -process reactions, particularly (α, n) , in the synthesis of light r-process nuclei. Our goal here is to discuss the main sources of theoretical uncertainty of calculated (α, n) reaction rates. Rather than discussing an extensive group of reactions, we focused on few important cases using two of the most popular reaction codes, namely TALYS [1] and NON-SMOKER [2].

The paper is structured in the following way: Sec. II summarizes the most important aspects of the α process. In Sec. III, we discuss the main sources of theoret-

ical uncertainties in the calculation of (α, n) reactions. First, the main theoretical aspects of NON-SMOKER and TALYS are described (Sec. III A). Their calculated rates for some specific reactions are compared and discussed. This is followed by a more detailed study of the sensitivity of the results to the technical aspects of these codes (Sec. III B), and to several nuclear properties, including alpha potentials, masses, level densities, optical potentials, pre-equilibrium intranuclear transition rates, level structure, radiative transmission coefficients, and width fluctuation corrections (Sec. III C). Summary and conclusions are given in Sec. IV.

II. THE α PROCESS IN NEUTRINO-DRIVEN WINDS

An attractive site where the α process (or charged-particle process) can occur is the neutrino-driven wind emitted during the cooling of a neutron star born after a core-collapse supernova explosion [9, 21–23].

When matter is still near the neutron star, the high temperatures maintain the abundances in nuclear statistical equilibrium (NSE). The initial composition is dominated by neutrons and protons that form α particles [9]. As matter expands and its temperature and density drop, α particles start to combine into heavier nuclei via $3\alpha \rightarrow {}^{12}\text{C}$ and $\alpha(\alpha, n){}^9\text{Be}(\alpha, n){}^{12}\text{C}$, followed by (α, n) , (n, γ) , (p, n) , and their inverse reactions. Since the fastest reactions (by several orders of magnitude) are $(n, \gamma) - (\gamma, n)$, the matter distribution within each element is accumulated at a few waiting-point isotopes, similarly to a hot r process. While these reactions are in statistical equilibrium, the isotopic abundance within a given element is determined by the temperature and neutron density of the environment. Since β decays are slow compared to the wind expansion time scale, nuclei increase their proton number by (α, n) and (p, n) captures. These reactions are in equilibrium with their inverse for $T \gtrsim 4$ GK. At lower temperatures, the (α, n) and (n, α) channels are out of equilibrium, and (α, n) reactions become the main mechanism to drive the synthesized matter towards heavier elements. Only at relatively long times (low temperatures), β decays become faster than charge-particle reactions. It should be pointed out that due to the fast expansion timescale, the drop in temperature occurs in a lapse of ≈ 10 ms and it is in that lapse that most of the nucleosynthesis heavier than Fe occurs.

III. THEORETICAL UNCERTAINTY OF (α, n) REACTIONS

Most of the α reaction rates involved in the α process must be calculated with reaction codes. Although the backbone of these codes is the reaction cross section given by the Hauser-Feshbach model [24], they can present substantial differences in three aspects:

First, there might be technical differences in the methods and algorithms used by these codes to solve the Hauser-Feshbach equations; we will refer to them as technical aspects. Second, the reaction codes can use different models and/or databases to extract the nuclear properties (nuclear inputs) entering into the calculation of the reaction rates. Third, some of the reaction codes include additional reaction mechanisms that go beyond the Hauser-Feshbach formalism, such as direct or pre-equilibrium components.

The apparent arbitrariness in the treatment of the reaction can be constrained to some extent by evaluating which options in the calculations are better suited to reproduce measured rates, whenever available. Unfortunately this is only possible for nuclei not too far from stability. For more exotic reactions like those typically involved in the α process, the differences in the calculated rates arising from the three aspects listed above give an idea of the so-called theoretical uncertainty. We have studied the main sources of theoretical uncertainty by comparing the calculated reaction rates of some selected important (α, n) cases, using different reaction codes and nuclear inputs.

A. TALYS and NON-SMOKER

In the present work, we have used TALYS (version 1.6) [1] as the main tool to evaluate the theoretical uncertainty of the (α, n) rates. Three were the reasons to chose this code: First, its source is open to the user, allowing a deep understanding of the implementation of the reaction sequence, as well as the modification of any part of the code. Second, besides calculating the compound-nucleus reactions to both discrete states and the continuum, TALYS uses the DBWA [25] and the coupled-channel theory [26] (for deformed nuclei) to calculate the direct reaction channel to discrete states, and the EXCITON model [27] to describe the pre-equilibrium component and the direct-to-continuum contribution. Third, TALYS includes the possibility to choose among different sources (models and/or databases) to determine the nuclear inputs. Table I lists the nuclear inputs and their sources considered in the present work; they are also discussed in the appendix. Our “baseline” calculations were done with TALYS using its default options for most of the nuclear inputs. Exceptions were the nuclear masses, which were taken from theoretical calculations instead of the Audi-Wapstra mass table (Audi 2003) [28], and the optical potentials, which were calculated using the global model [1] instead of the local formulation [27]. The resulting packet of options, referred to as TALYS 1, is summarized in Table II (the packet TALYS 2 included in the table is introduced in Sec. III B).

For the sake of completeness, we have included in our study the rates published in the NON-SMOKER database [2]. We chose this code because it has been extensively used in many sensitivity studies involving

TABLE I: List of the nuclear inputs considered in the present work (first column) and the different sources available for their determination (second column). The third column indicates the label used throughout the text to refer to the corresponding source. A description of the different nuclear-input sources can be found in the appendix.

Nuclear input	Source	Label	Refs.
Alpha optical potential	Global model	GAOP	[1]
	McFadden-Satchler model	MS	[29]
	Demetriou-Grama-Goriely model 1	DGG1	[30]
	Demetriou-Grama-Goriely model 2	DGG2	[30]
	Demetriou-Grama-Goriely model 3	DGG3	[30]
Mass (and deformation)	Finite-range droplet model	FRDM	[31]
	Skyrme-Hartree-Fock-Bogoliubov	SHFB	[32]
	Gogny-Hartree-Fock-Bogoliubov	GHFB	[33]
	2003 Audi-Wapstra mass table	EXP	[28]
Level density	Constant temperature model	CTM	[1, 34]
	Back-shifted Fermi gas model	BFM	[1, 35]
	Generalized superfluid model	GSM	[1, 36]
	Statistical microscopic model	SMM	[1, 35]
	Combinatorial microscopic model	CMM	[1, 37]
	Rauscher-Thielemann-Kratz model	RTK ^a	[38]
Proton/neutron optical potential	Global model	GOP	[1]
	Bauge-Delaroche-Girod model	BDG0	[1, 39]
	Bauge-Delaroche-Girod model 1	BDG1	[1, 39]
	Bauge-Delaroche-Girod model 2	BDG2	[1, 39]
	Bauge-Delaroche-Girod model 3	BDG3	[1, 39]
	Jeukenne-Lejeunne-Mahaux model	JLM ^b	[40–42]
Pre-equilibrium	Exciton model 1	PREEQ1	[1, 27]
	Exciton model 2	PREEQ2	[1, 27]
	Exciton model 3	PREEQ3	[1, 27]
	Multi-step compound model	PREEQ4	[1, 27]
	Pre-equilibrium disabled	NO PREEQ	
Level structure	Reference Input Parameter Library	RIPL	[43]
	RIPL + theoretical extension	RIPL+th	[1, 43]
	Firestone’s Table of Isotopes, 8 th edition	FTI ^b	[44]
Radiative transmission coefficient	Brink-Axel formula	BA	[45]
	Kopecky-Uhl formula	KU	[46]
	Hartree-Fock BCS tables	HF-BCS	[1]
	Hartree-Fock-Bogolyubov tables	HFB	[1]
	Goriely’s hybrid model	GH	[47]
	Cowan-Thielemann-Truran model	CTT ^a	[48]
Width fluctuation correction	Hofmann-Richert-Tepel-Weidenmüller model 1	HRTW1	[49, 50]
	Hofmann-Richert-Tepel-Weidenmüller model 2	HRTW2	[49, 51]
	Moldauer model	Moldauer	[52]
	Gaussian orthogonal ensemble of Hamiltonian matrices	GOE	[53]
	Width fluctuation correction disabled	No WFC	

^aModel implemented in the present work, but not originally included in TALYS.

^bOption not included in TALYS.

neutron-capture reactions (e.g. [13, 17]). Unlike TALYS, NON-SMOKER does not include the pre-equilibrium or direct components. Moreover, each code uses their own group of models and tables to determine the nuclear inputs, as shown in Table II.

Before analyzing in detail the theoretical uncertainties of reactions involved in the α process, it is important to know the degree of validity of these codes by comparing their predictions with several experimentally known (α, n) rates. Fig. 1 includes the measured rates for the reactions $^{21}\text{Ne}(\alpha, n)^{24}\text{Mg}$ [54], $^{25}\text{Mg}(\alpha, n)^{28}\text{Si}$ [54], and $^{41}\text{K}(\alpha, n)^{44}\text{Sb}$ [55], compared with the results calculated with TALYS using the default packet of nuclear-inputs TALYS 1, and the rates from NON-SMOKER. The differences between the calculations and measurements can be seen in more detail by analyzing the ratios between theoretical-to-measured rates; they are included in Fig. 1 for the reaction $^{21}\text{Ne}(\alpha, n)^{24}\text{Mg}$ (b), $^{25}\text{Mg}(\alpha, n)^{28}\text{Si}$ (d), and $^{41}\text{K}(\alpha, n)^{44}\text{Sb}$ (f).

Overall, it is fair to say that both models do reasonably well: For $^{21}\text{Ne}(\alpha, n)^{24}\text{Mg}$, the NON-SMOKER (dotted green line) and TALYS 1 (red solid line) rates are almost identical, both showing maximum deviations from the experimental data (about 60%) at low temperatures ($T \simeq 2$ GK), and better agreement at higher temperatures. For $^{25}\text{Mg}(\alpha, n)^{28}\text{Si}$, both models give similar results at temperatures below $T \simeq 2$ GK, agreeing with the measured data at $T < 1.5$ GK, and deviating up to 50% at 2 GK. At higher temperatures, NON-SMOKER gets gradually closer to the measured data whereas TALYS 1 overestimates them by about 60%. For $^{41}\text{K}(\alpha, n)^{44}\text{Sb}$, the TALYS 1 rates are too high for T between 1.5 GK and 6 GK, and too low for T greater than 6 GK. A more precise quantitative comparison is not possible for this reaction because the authors did not include the experimental uncertainty for the measured rates. Unfortunately the rates for this reaction are not included in the NON-SMOKER database [2].

B. Sensitivity of calculated rates to technical aspects

As mentioned in the beginning of Sec. III, the theoretical uncertainty in the calculated reaction rates arises from 1) the different technical aspects (i.e. algorithms and methods used to solve the Hauser-Feshbach equations), 2) the ambiguity in the choice of nuclear inputs, and 3) the inclusion (in some codes) of “secondary” reaction mechanisms that go beyond the Hauser-Feshbach formalism.

In the first part of our study, discussed in this section, we focus on the first source of uncertainty, i.e. that due to technical aspects. Our approach was to create a new TALYS packet (TALYS 2), which uses the same (or similar) nuclear-inputs sources than NON-SMOKER, and compare the rates from both codes for some selected reactions. Although NON-SMOKER is

a closed-source code, the models and methods used to calculate its nuclear inputs are extensively described in Refs. [38, 56]. In principle, most of the nuclear-input sources used by NON-SMOKER are available in TALYS, either the same model/database or at least a similar version. For instance, the new packet TALYS 2 included the Bauge-Delaroche-Girod model [39] for the proton/neutron optical potential, which is very similar to the Jeukenne-Lejeune-Mahaux optical potential model used in NON-SMOKER [40–42] (see appendix for more details). For some especial cases (level densities, radiative transmission coefficients, and width fluctuations), we had to modify the TALYS source code to include the same models than NON-SMOKER, as discussed in the appendix. In addition, we also disabled the calculation of the pre-equilibrium component, which, as stated above, also accounts for direct reactions to the continuum. The set of nuclear-input sources used to define the new packet TALYS 2 is compared in Table II with the sets used in TALYS 1 and NON-SMOKER. Note that although TALYS 2 still includes the direct component to discrete states (ignored in NON-SMOKER), the contribution from this channel is negligible in the range of energies considered here. The results from TALYS 2 are shown in Fig. 1 (solid-dotted blue line) for the reactions $^{21}\text{Ne}(\alpha, n)^{24}\text{Mg}$, $^{25}\text{Mg}(\alpha, n)^{28}\text{Si}$, and $^{41}\text{K}(\alpha, n)^{44}\text{Sb}$. As expected, in spite of using the similar nuclear-input sources and reaction mechanisms, the results from TALYS 2 and NON-SMOKER differ from each other due to differences in technical aspects.

In order to analyze the theoretical uncertainties of (α, n) rates in the α process, we used the reaction $^{86}\text{Se}(\alpha, n)^{89}\text{Kr}$ as an illustrative example. Our sensitivity studies of (α, n) rates have shown that this reaction has significant impact in the synthesis of the light r-process nuclei [57]. The rates taken from NON-SMOKER and the two TALYS packets (TALYS 1 and TALYS 2) are shown in Fig. 2(a) for different temperatures T . In order to better illustrate the differences between the calculations, Fig. 2(b) shows the rates normalized to TALYS 1. At $T \lesssim 2$ GK, the NON-SMOKER rates (green dotted line) are almost 10 times lower than TALYS 1 (red solid line), and about 50% lower than TALYS 2 (blue dash-dotted line). This reduction of the differences between TALYS 2 and NON-SMOKER at low T is entirely due to the fact they use the same set of nuclear-input sources. At higher temperatures, the rate ratio NON-SMOKER to TALYS 1 exhibit a systematic increase, reaching maximum deviations of up to four orders of magnitude at $T=10$ GK. Although the results from TALYS 2 are closer to NON-SMOKER, the differences at high temperatures are still very large (three orders of magnitude at $T=10$ GK). After careful consideration of this striking feature, we noticed that the (α, n) reaction rates published in the NON-SMOKER database are actually inclusive, i.e. they include the emission of multiple neutrons [e.g. $(\alpha, 2n)$, $(\alpha, 3n)$, etc.] accompanying the one-neutron channel $(\alpha, 1n)$. On the contrary,

TABLE II: List of nuclear inputs considered in the present study and the corresponding sources (models or databases) used in TALYS (packets TALYS 1 and TALYS 2) and NON-SMOKER. The sources are referred to by the labels included in Table I.

Nuclear Input	TALYS 1	NON-SMOKER	TALYS 2
Alpha optical potential (AOP)	GAOP	MS	MS
Mass (and deformation)	SHFB	FRDM	FRDM
Level density	CTM	RTK ^a	RTK ^a
Proton/neutron optical potential	GOP	JLM ^b	BDG0
Pre-equilibrium	PREEQ2	NO PREEQ	NO PREEQ
Level structure	RIPL+th	FTI ^b	RIPL
Radiative transmission coefficient	KU ^c	CTT ^{a,d}	CTT ^{a,d}
Width fluctuation correction	Moldauer	HRTW2 ^a	HRTW2 ^a

^aOption implemented in the present work, but not originally included in TALYS.

^bOption not included in TALYS.

^c $E1$, $M1$, $E2$, and $M2$ transitions included.

^d $E1$ and $M1$ transitions included.

the TALYS rates discussed so far correspond to the exclusive ($\alpha, 1n$) channel, which is explicitly considered in nucleosynthesis network calculations. In principle, the difference between inclusive (α, n) and exclusive ($\alpha, 1n$) rates is negligible at low energies or for light systems, where the Q -values for ($\alpha, \times n$), with $\times > 1$, are very high. Such is the case with the reactions $^{21}\text{Ne}(\alpha, n)^{24}\text{Mg}$ and $^{25}\text{Mg}(\alpha, n)^{28}\text{Si}$ shown in Figs. 1(b),(d), where the inclusive (α, n) rates from NON-SMOKER are very close to the TALYS exclusive ($\alpha, 1n$) channel. However, for heavier systems, other contributing channels become important at high temperatures. This is illustrated in Fig. 3(a), where we show the TALYS 1 reaction rates for the most important exclusive channels contributing to the inclusive reaction rate of $^{86}\text{Se}(\alpha, n)$. Note that the ($\alpha, 2n$), ($\alpha, 3n$), and ($\alpha, 4n$) rates become higher than ($\alpha, 1n$) at $T \simeq 3.5$ GK, $\simeq 6$ GK, and $\simeq 7.5$ GK respectively. In order to compare the $^{86}\text{Se}(\alpha, n)$ inclusive reaction rates from TALYS and NON-SMOKER, we show in Fig. 3(b) the inclusive rates from TALYS 2 and NON-SMOKER normalized to the inclusive rates from TALYS 1. As can be seen, the large differences at high T seen in Fig. 2 between the TALYS and NON-SMOKER rates are reduced to less than a factor 10 when the former includes all the channels contributing to the inclusive reaction. We have compared the rates from TALYS and NON-SMOKER for other important (α, n) reaction, and observed the same behavior at high temperatures. Fig. 4(a) shows the TALYS 1 inclusive rates with the most important exclusive channels for the reaction $^{74}\text{Ga}(\alpha, n)$. The inclusive rates from TALYS (TALYS 1 and TALYS 2) are compared with the results from NON-SMOKER in Fig. 4(b) for the same reaction.

Another technical aspect contributing to the differences between TALYS and NON-SMOKER at high T is the binning of the excitation energy grid. The equidistant binning used in previous versions of TALYS (e.g. version 1.4 [58]) was replaced in the current TALYS version 1.6 [1] (used in the present work) by a more efficient

logarithmic binning for the excitation energy grid. In Fig. 5(a), we compare the $^{86}\text{Se}(\alpha, n)$ rates from NON-SMOKER with the inclusive rates from TALYS (TALYS 1 and TALYS 2) using the current logarithmic binning and the old equidistant binning. It is striking to see the impact that the binning method has in the TALYS results at high temperatures. The fact that the TALYS rates calculated with the equidistant binning match the results from NON-SMOKER at high T indicates that the later likely uses a similar binning method. The same result was observed for other important (α, n) reactions, as shown in Fig. 5(b) for the reaction $^{74}\text{Ga}(\alpha, n)$.

The results discussed here prove that we understand the most important differences between TALYS and NON-SMOKER: Our starting point was Fig. 2(b), where the TALYS 1 (red solid line) and NON-SMOKER (green dotted line) rates reach deviations of one order of magnitude at $T=1$ GK and four orders of magnitude at $T=10$ GK. The differences at low temperatures are almost entirely due to the nuclear-input sources of each code. Indeed, switching the TALYS packet from TALYS 1 to TALYS 2—using similar nuclear-input models and reaction mechanisms (i.e. no pre-equilibrium component) than NON-SMOKER—significantly reduced the differences between TALYS and NON-SMOKER. At higher temperatures, the large differences between TALYS 1 and NON-SMOKER are due to 1) the fact that the rates from NON-SMOKER are actually inclusive, and 2) the new logarithmic-binning algorithm used in the new TALYS version 1.6 to track the excitation energies. This is also observed for other important reactions like $^{74}\text{Ga}(\alpha, n)$.

Before closing this section, it is important to emphasize that the use of NON-SMOKER (α, n) rates may induce to errors if one assumes that they correspond to the exclusive channel ($\alpha, 1n$), typically used in network calculations. However, we expect a moderate effect at the temperatures relevant for the α process (i.e. in the range $\simeq 1$ –4 GK) where the ($\alpha, 1n$) channel is dominant. As for

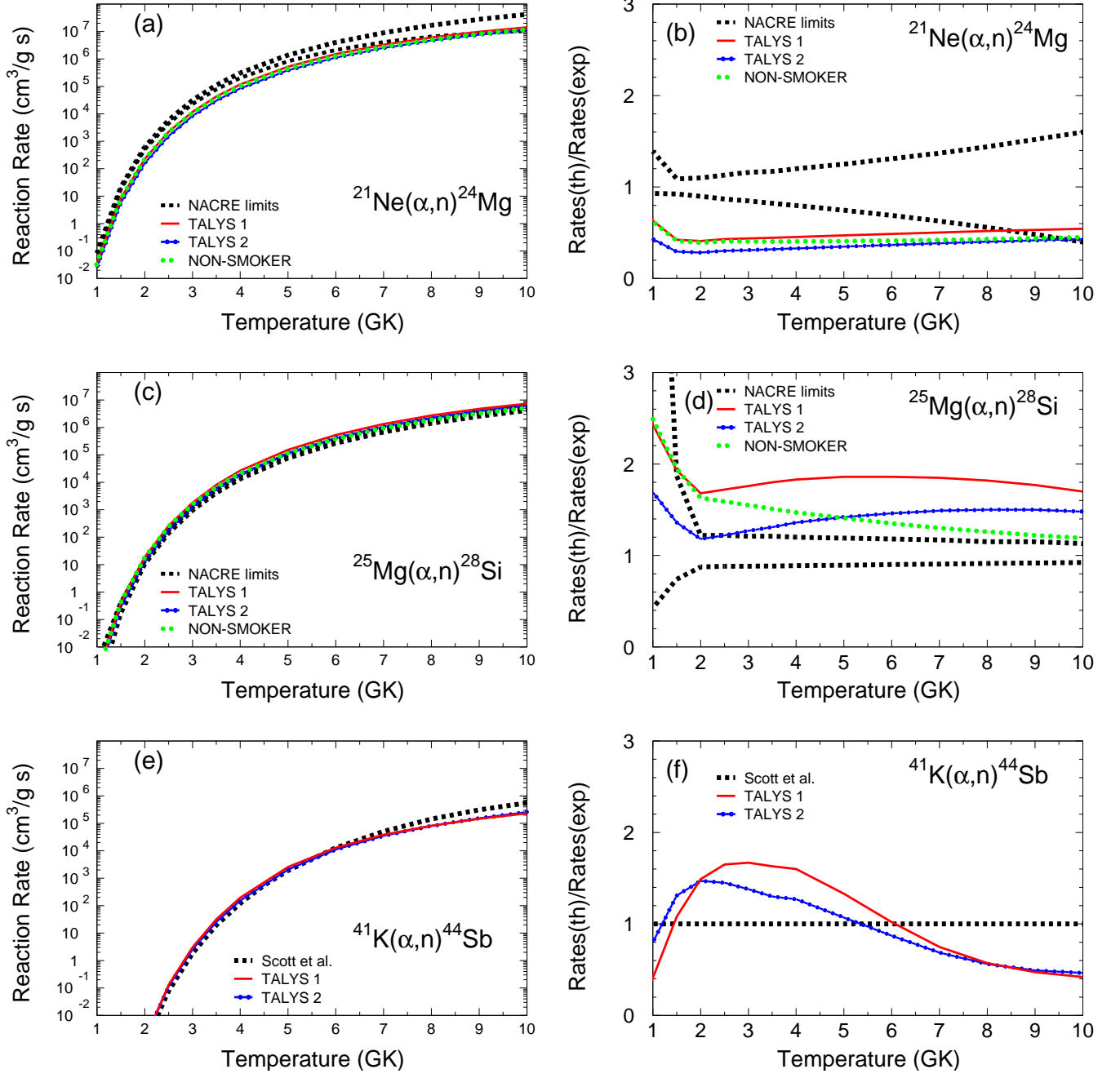


FIG. 1: (Color online) Nuclear reaction rates (a) and ratio of theoretical-to-experimental rates (b) for the reaction $^{21}\text{Ne}(\alpha, n)^{24}\text{Mg}$ as a function of temperature. The black dashed lines delimit the experimental uncertainty. The calculated rates correspond to NON-SMOKER (green dotted line), and TALYS using the default packet of nuclear inputs TALYS 1 (red solid line), and the packet TALYS 2 explained in Sec. IIIB (blue solid-dotted line). Figures (c) and (d): Same as (a) and (b) for the reaction $^{25}\text{Mg}(\alpha, n)^{28}\text{Si}$. Figures (e) and (f) Same as (a) and (b) for the reaction $^{41}\text{K}(\alpha, n)^{44}\text{Sb}$. The experimental rates for $^{21}\text{Ne}(\alpha, n)^{24}\text{Mg}$ and $^{25}\text{Mg}(\alpha, n)^{28}\text{Si}$ were taken from the NACRE database [54]. The rates for $^{41}\text{K}(\alpha, n)^{44}\text{Sb}$ were measured by Scott *et al.* [55] (note that these authors reported only the uncertainty of the cross sections, not the rates).

the energy binning, it is very important to measure the inclusive rates of the reactions discussed above at high temperatures in order to verify that the new logarithmic

binning improves indeed the theoretical results.

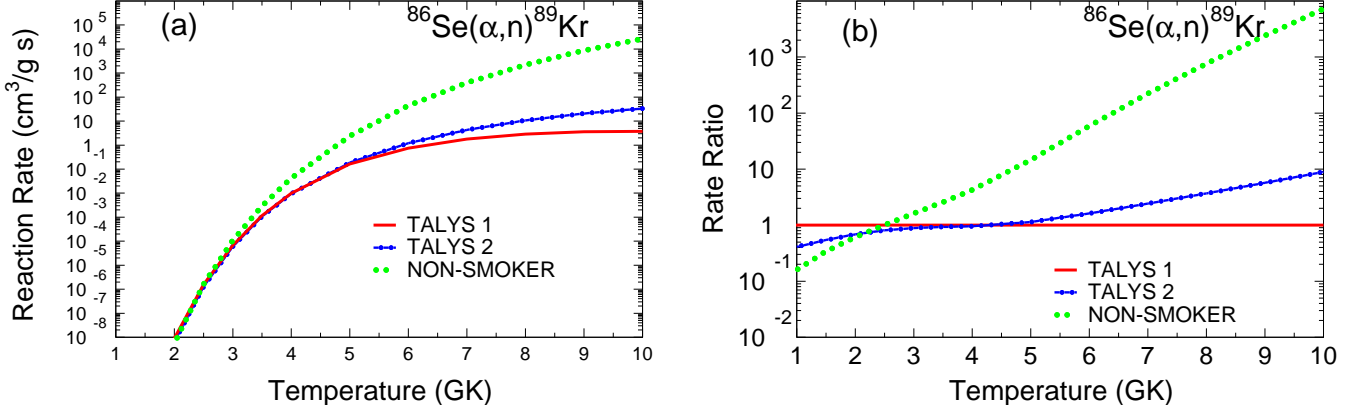


FIG. 2: (Color online) (a) TALYS and NON-SMOKER nuclear rates for the reaction $^{86}\text{Se}(\alpha, n)^{89}\text{Kr}$. The TALYS rates were obtained using the packets TALYS 1 and TALYS 2 summarized in Table II. (b) NON-SMOKER and TALYS 2 rates normalized to the results from TALYS 1.

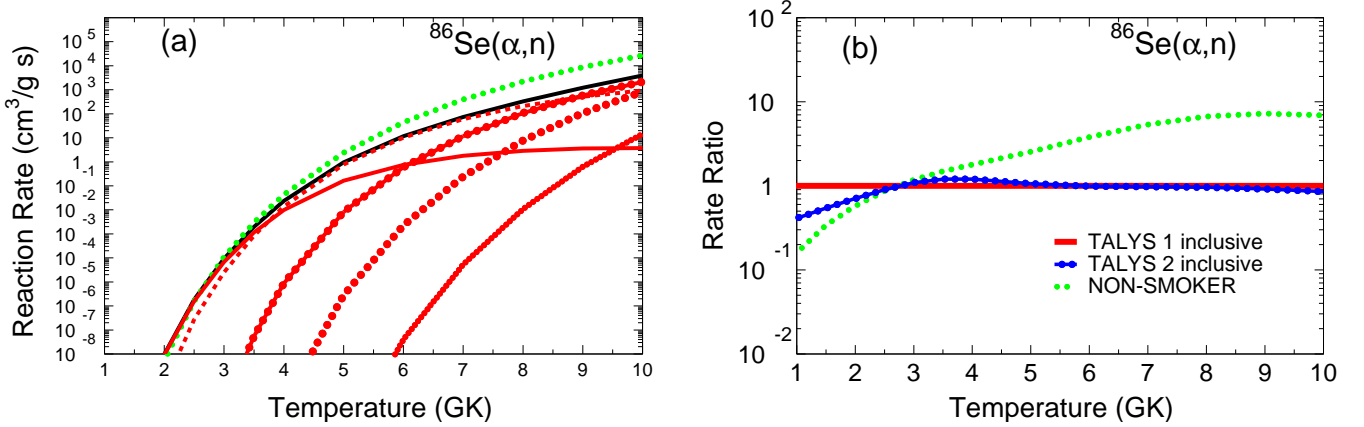


FIG. 3: (Color online) (a) Decompositions of the $^{86}\text{Se}(\alpha, n)$ inclusive reaction rate from TALYS 1 (black solid line) into the main contributing channels $^{86}\text{Se}(\alpha, \times n)$, where $\times=1$ (solid red line), $\times=2$ (dashed red line), $\times=3$ (solid-dotted red line), $\times=4$ (thick dotted red line), and $\times=5$ (thin dotted red line); the NON-SMOKER rates are shown by the green dotted line. (b) Calculated $^{86}\text{Se}(\alpha, n)$ inclusive rates normalized to TALYS 1 inclusive rates. Red thick solid line: inclusive (α, n) from TALYS 1; blue thick solid-dotted line: inclusive (α, n) from TALYS 2; green dotted line: (α, n) from NON-SMOKER.

C. Sensitivity of calculated rates to nuclear physics properties

The differences between the TALYS and NON-SMOKER results discussed so far give an idea of the theoretical uncertainty arising from technical aspects related to the implementation of the reaction sequence. In this section, we discuss the sensitivity of the $^{86}\text{Se}(\alpha, n)^{89}\text{Kr}$ reaction rates from TALYS to the most important nuclear properties (nuclear inputs), namely alpha optical potentials, level densities, nuclear masses, proton and neutron optical potentials, pre-equilibrium, nuclear structure, radiative transmission coefficients, and width fluctuation corrections. We focused on one input at a time. Our

approach was to calculate the rates of $^{86}\text{Se}(\alpha, n)^{89}\text{Kr}$ using TALYS 1 (Table II), except for the selected nuclear input, which was taken from the different models listed in Table I. The results discussed below are included in Fig 6(a)-(f).

1. Alpha optical potential

In TALYS, the alpha optical potential (AOP) has a strong effect in the calculated reaction rates. First, and most important, the compound-nucleus contribution depends directly on the AOP via the transmission coefficients, calculated by solving the Schrödinger equation. Second, the composite-nucleus formation cross section,

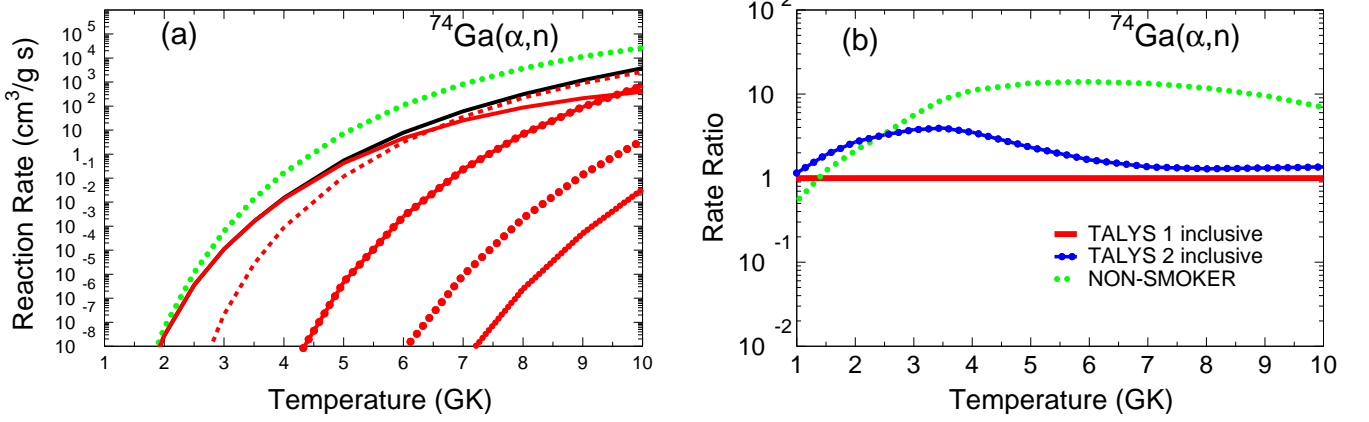


FIG. 4: (Color online) (a) Decompositions of the $^{74}\text{Ga}(\alpha, n)$ inclusive reaction rate from TALYS 1 (black solid line) into the main contributing channels $^{74}\text{Ga}(\alpha, \times n)$, where $\times=1$ (solid red line), $\times=2$ (dashed red line), $\times=3$ (solid-dotted red line), $\times=4$ (thick dotted red line), and $\times=5$ (thin dotted red line); the NON-SMOKER rates are shown by the green dotted line. (b) Calculated $^{74}\text{Ga}(\alpha, n)$ inclusive rates normalized to TALYS 1 inclusive rates. Red thick solid line: inclusive (α, n) from TALYS 1; blue thick solid-dotted line: inclusive (α, n) from TALYS 2; green dotted line: (α, n) from NON-SMOKER.

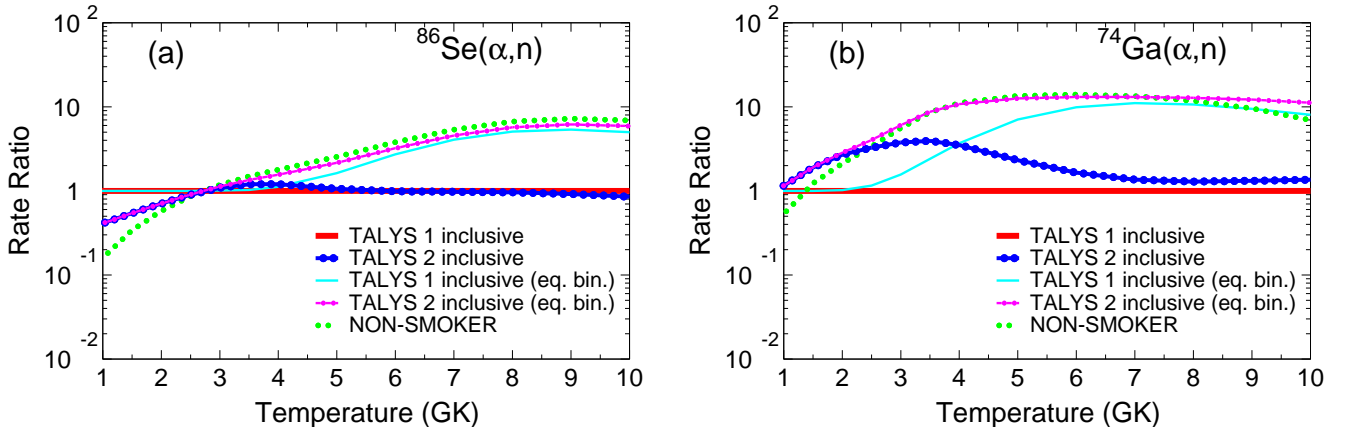


FIG. 5: (Color online) (a) Calculated $^{86}\text{Se}(\alpha, n)$ inclusive rates normalized to TALYS 1 inclusive rates. Red thick solid line: inclusive (α, n) from TALYS 1; blue thick solid-dotted line: inclusive (α, n) from TALYS 2; green dotted line: (α, n) from NON-SMOKER; light-blue thin solid line: inclusive (α, n) from TALYS 1 using the equidistant energy binning; purple solid-dotted line: inclusive (α, n) from TALYS 2 using the equidistant energy binning. (b) Same as (a) for the reaction $^{74}\text{Ga}(\alpha, n)$. (See text for details.)

necessary to determine the pre-equilibrium component, is given by the difference between the reaction cross section and the direct cross section into discrete states, both of which depend on the AOP. Finally, the AOP of the target nucleus affects directly the direct reaction component through the coupled-channel (CC) formalism (for deformed nuclei), or the Distorted Wave Born Approximation (DWBA) (for spherical nuclei).

As an illustrative example of the sensitivity of TALYS rates to AOP, we compare in Fig. 6(a) the rates of the reaction $^{86}\text{Se}(\alpha, n)^{89}\text{Kr}$ calculated with TALYS using the AOP models listed in Table I, and the packet TALYS 1 for the rest of the nuclear inputs (see Table II). The rates

are normalized to the results obtained using the default packet TALYS 1 for all the nuclear inputs.

For the temperatures relevant for the α process ($T \lesssim 4$ GK), the differences between the results are in the range of 1-to-2 orders of magnitude. The maximum deviations are seen between the results calculated with the GAOP (used in TALYS 1) and DDG3 models. The disagreement between the AOP models are gradually reduced as the temperature increases. Beyond $T \simeq 5$ GK the differences are about 30%.

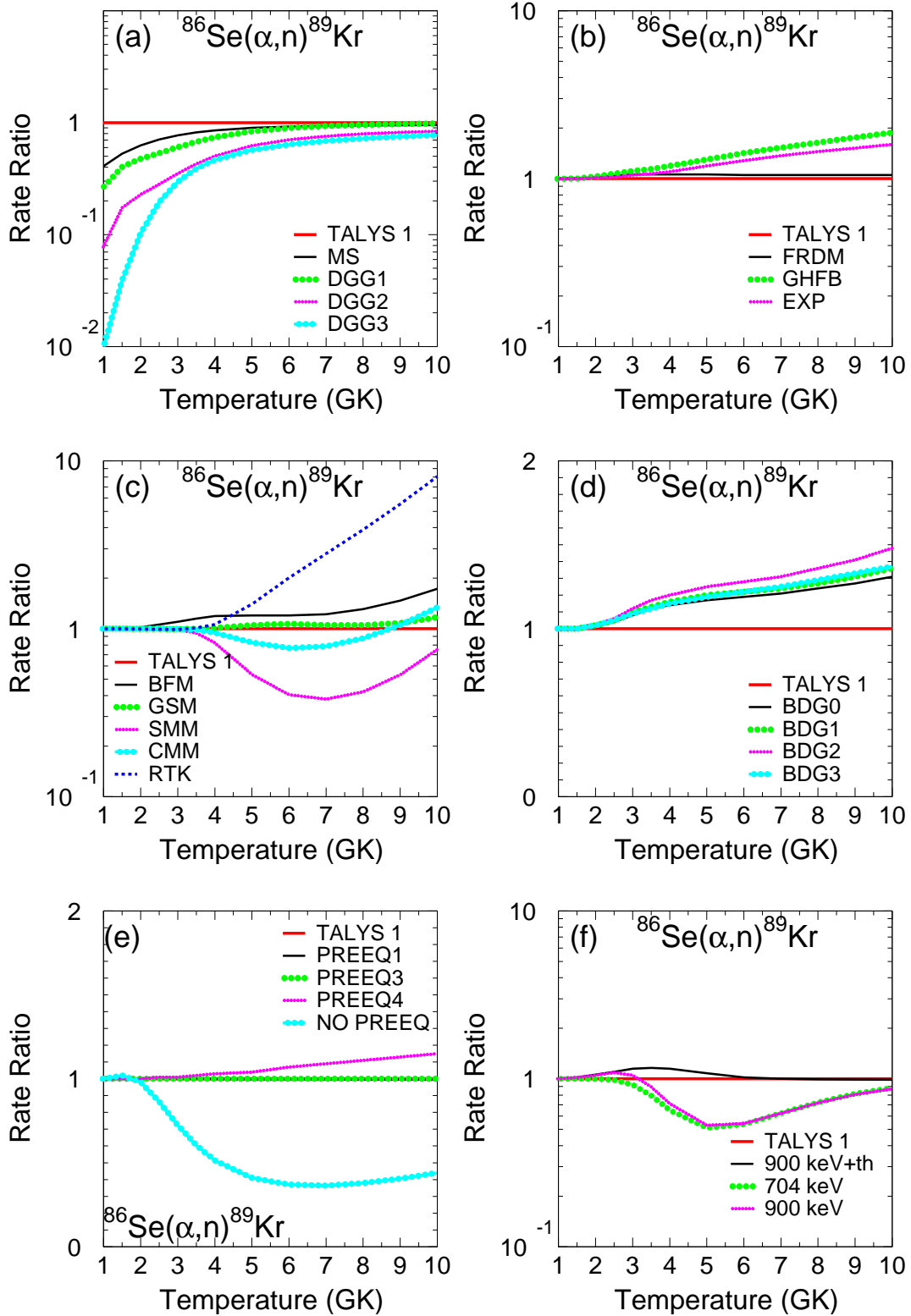


FIG. 6: (Color online) TALYS rates for $^{86}\text{Se}(\alpha, n)^{89}\text{Kr}$. The calculations were done using the nuclear models of packet TALYS 1 (Table II) except for the nuclear input investigated [(a) alpha optical potentials, (b) masses, (c) level densities, (d) proton/neutron optical potentials, (e) pre-equilibrium, (f) level structure] which were determined from the models/options listed in Table I and the appendix. All the rates are normalized to the values obtained using the packet TALYS 1 for all the nuclear inputs. The labels included in the legend are described in Table I. (See text for details.)

2. Nuclear mass

The sensitivity of TALYS to the selected mass model rests on the particle separation energies used to determine other quantities like the Fermi energy, excitation energies and temperatures of the nuclei involved in the reaction, the total energy of the compound nucleus, etc. These energies enter in the calculation of e.g. the optical potentials, pre-equilibrium emission and internal transition rates, compound-nucleus transmission coefficients and level densities. Furthermore, TALYS uses the ground-state deformations predicted by the selected mass model.

In Fig. 6(b), we show the rates of the reaction $^{86}\text{Se}(\alpha, n)^{89}\text{Kr}$ calculated with TALYS taking the masses from the models and options listed in Table I, and using the packet TALYS 1 for the rest of the nuclear inputs (see Table II). The rates are normalized to the results obtained using the default packet TALYS 1 for all the nuclear inputs.

One sees that the differences between the rates obtained with the SHFB (used in TALYS 1) and FRDM mass models are negligible. The results obtained with the GHFB model or the 2003 Audi-Wapstra mass table [28] are higher than TALYS 1, reaching maximum deviations (about a factor 2) at the highest temperatures.

3. Level density

The dependence of the TALYS-calculated rates on the level density arises mostly from the transmission coefficients of exit channels populating energies in the continuum or above the last known discrete level. In addition (although less important for the present work) the width of the gamma-ray strength function is mostly given by s-wave radiation width, which is related to the density of final states that can be reached in the first step of the gamma cascade.

We show in Fig. 6(c) the TALYS rates for the reaction $^{86}\text{Se}(\alpha, n)^{89}\text{Kr}$ using the level densities listed in Table I, and the packet TALYS 1 for the rest of the nuclear inputs (see Table II). As explained in the appendix, we had to code the RTK model (used by NON-SMOKER) in order to include it in TALYS. Again, all the rates are normalized to the results obtained using TALYS 1 for all the nuclear inputs.

In general, we see that the different calculations give similar results in the range of temperatures relevant for the α process, i.e. $T \lesssim 4$ GK. The rates from the RTK model increase at higher temperatures, reaching maximum deviations of a factor 10 with respect to the CTM (used in TALYS 1). The maximum differences observed with the other level-density models are significantly smaller (about 60%).

4. Proton and neutron optical potential

In (α, n) reactions, the neutron and proton OP are necessary to determine the transmission coefficients for the compound-nucleus component; the inverse cross sections used to calculate the pre-equilibrium emission rates, and knockout and transfer reactions; and the reaction cross section determining the normalization of the compound-nucleus cross section. In addition, as explained in the appendix, TALYS includes an option to calculate the pre-equilibrium intranuclear transition rates by averaging the imaginary part of the optical potential depth.

Fig. 6(d) shows the TALYS rates for the reaction $^{86}\text{Se}(\alpha, n)^{89}\text{Kr}$ obtained with the different OP models listed in Table I, and the packet TALYS 1 for the rest of the nuclear inputs (see Table II). All the rates are normalized to the results obtained using TALYS 1 for all the nuclear inputs.

The differences observed between the models are very small (less than 20%) in the range of temperatures $T \simeq 1$ -4 GK relevant for the α process, whereas they gradually increase at higher temperatures, reaching maximum values up to 50% at 10 GK.

5. Pre-equilibrium

As explained in the appendix, in the present work we have considered four different pre-equilibrium models implemented in TALYS.

Fig. 6(e) shows the TALYS rates of the reaction $^{86}\text{Se}(\alpha, n)^{89}\text{Kr}$ obtained with the pre-equilibrium options listed in Table I, and using the packet TALYS 1 for the rest of the nuclear inputs (see Table II). The rates are normalized to the values obtained with the packet TALYS 1 for all the nuclear inputs.

The method used to determine the intranuclear transition rates [PREEQ1, PREEQ2 (used in TALYS 1), and PREEQ3] has minimal impact in the results. Considering pre-equilibrium for the first binary collision (PREEQ4) increases the rates by about 15% at the highest temperatures. On the other hand, disabling pre-equilibrium reduces the rates by about 50% for temperatures above 4 GK.

6. Structure

The level structure (energy, spin, and parity) of the nuclei involved in the reaction is crucial in the determination of the reaction rate. First, the calculation of the compound-nucleus cross section is done by summing up the transmission coefficients (which depend on energy, spin, and parity) over the spin and parities of all the energetically possible states. Second (and less important for the present study) the low-energy levels are important in the coupled-channel model to determine the direct cross section of deformed nuclei. Apart from this

explicit level-structure dependence, whenever the excitation energies of the residue nucleus are greater than the last experimentally-known level, the sum of transmission coefficients over spins and parities must be replaced by an integral over the level density. Beard *et al.* studied this “truncation” effect by varying the maximum number of known levels in their calculations and found that their Maxwellian-averaged neutron-capture cross sections changed by almost 20% [13].

The TALYS calculations shown in Fig. 6(f) are all based on the packet TALYS 1, but differ on the level scheme of ^{86}Se and other nuclei accessible through the open channels in the reaction $^{86}\text{Se}(\alpha, n)^{89}\text{Kr}$. As explained in the appendix, the calculation labeled TALYS 1 (red line) takes up to 100 levels for each nucleus, including the experimentally known levels from the RIPL-3 database [43] and a theoretical extension based on the level density. In the case of ^{86}Se , the experimentally known excited levels included are 2_1^+ , 4_1^+ , and 6_1^+ with energies 704 keV, 1568 keV, and 2073 keV, respectively. The second calculation, labeled as “900 keV + th” (black line) is like TALYS 1, but with the 704-keV energy of the 2_1^+ level changed to an arbitrary value 900 keV. As can be seen, this change leads to a very small increase in the rates at $T \simeq 3$ GK.

In order to study the truncation effect described above, we repeated these two calculations using the same truncation scheme than NON-SMOKER, i.e., we disabled the theoretical extension of the level scheme, and limit the maximum number of experimental levels of all nuclei involved in the reaction to 19. Thus, the calculation labeled “704 keV” (thick green dotted line) used only the measured level scheme from RIPL-3 (including the 704-keV 2_1^+ energy for ^{86}Se), whereas the calculation labeled “900 keV” (thin purple dotted line) is like “704 keV”, but with the energy of the 2_1^+ level changed from 704 keV to 900 keV. As can be seen, the change in the truncation scheme reduces the rates by nearly 50% at temperatures around 5 GK, whereas the change of the 2_1^+ energy has an almost negligible effect.

7. Other nuclear inputs

Besides the nuclear inputs discussed above, we also studied the sensitivity of the TALYS rates to the radiative transmission coefficients T_γ and the width fluctuation correction WFC of the compound-nucleus contribution. The former is important for the description of the gamma emission channel, particularly at low energies where particle emission may be energetically disfavored. The WFC is important at rather low energies and results mostly in an enhancement of the elastic channel.

In the present work, we run several calculations using the models listed in Table I (and explained in the appendix), for T_γ and WFC, and the packet TALYS 1 for the rest of the nuclear inputs (see Table II). The differences between the different calculations were negligible

over the entire range of temperatures considered ($T=1-10$ GK).

8. Sensitivity of other $\text{Se}(\alpha, n)$ reactions to the alpha optical potential

Since the alpha optical potential is the nuclear input with the strongest effect in the range of temperatures relevant for the α process, we made a systematic study of the sensitivity of TALYS (α, n) rates to different AOP models for different Se isotopes. Like in previous sections, the nuclear inputs were taken from the packet TALYS 1 (Table II), except the alpha optical potentials which were calculated with the models listed in Table I.

Fig. 7 shows the results for the reactions $^{82}\text{Se}(\alpha, n)^{85}\text{Kr}$ (a), $^{83}\text{Se}(\alpha, n)^{86}\text{Kr}$ (b), $^{84}\text{Se}(\alpha, n)^{87}\text{Kr}$ (c), and $^{85}\text{Se}(\alpha, n)^{88}\text{Kr}$ (d). The rates are normalized to the results obtained using the packet TALYS 1 for all the nuclear inputs.

Like in the $^{86}\text{Se}(\alpha, n)^{89}\text{Kr}$ case, all the reactions show a strong sensitivity to the AOP models used in the calculations in the range of temperatures 1–4 GK relevant for the α process.

IV. SUMMARY AND CONCLUSIONS

The present work aims at studying the theoretical uncertainty in (α, n) reaction rates which are of crucial importance in the synthesis of light r-process nuclei (between Fe and Ag) through the α process.

Since most of the (α, n) reactions involved in the α process have not been measured, abundance network calculations rely on reaction codes to determine the corresponding rates. Although these codes follow the Hauser-Feshbach formalism, they can differ in 1) technical aspects related to the algorithms and methods used to calculate the reaction rates, 2) the sources (models or databases) used to determine the properties of the nuclei involved in the reaction, and 3) the inclusion of additional reaction mechanisms beyond the Hauser-Feshbach formalism.

In the first part of the paper, we focused on the theoretical uncertainty arising from technical aspects. Apart from the standard set of default nuclear-inputs sources included in TALYS (which we called TALYS 1), we defined a new TALYS packet (labeled TALYS 2) that uses the same nuclear-input sources than NON-SMOKER, and excludes the preequilibrium and direct-to-continuum components included in TALYS by default. By comparing the TALYS 2 and NON-SMOKER rates for the reaction $^{86}\text{Se}(\alpha, n)^{89}\text{Kr}$, we could determine the most important technical differences between both codes. The largest differences were found at high temperatures, where the TALYS 2 rates were up to three orders of magnitude lower than the results from NON-SMOKER. We

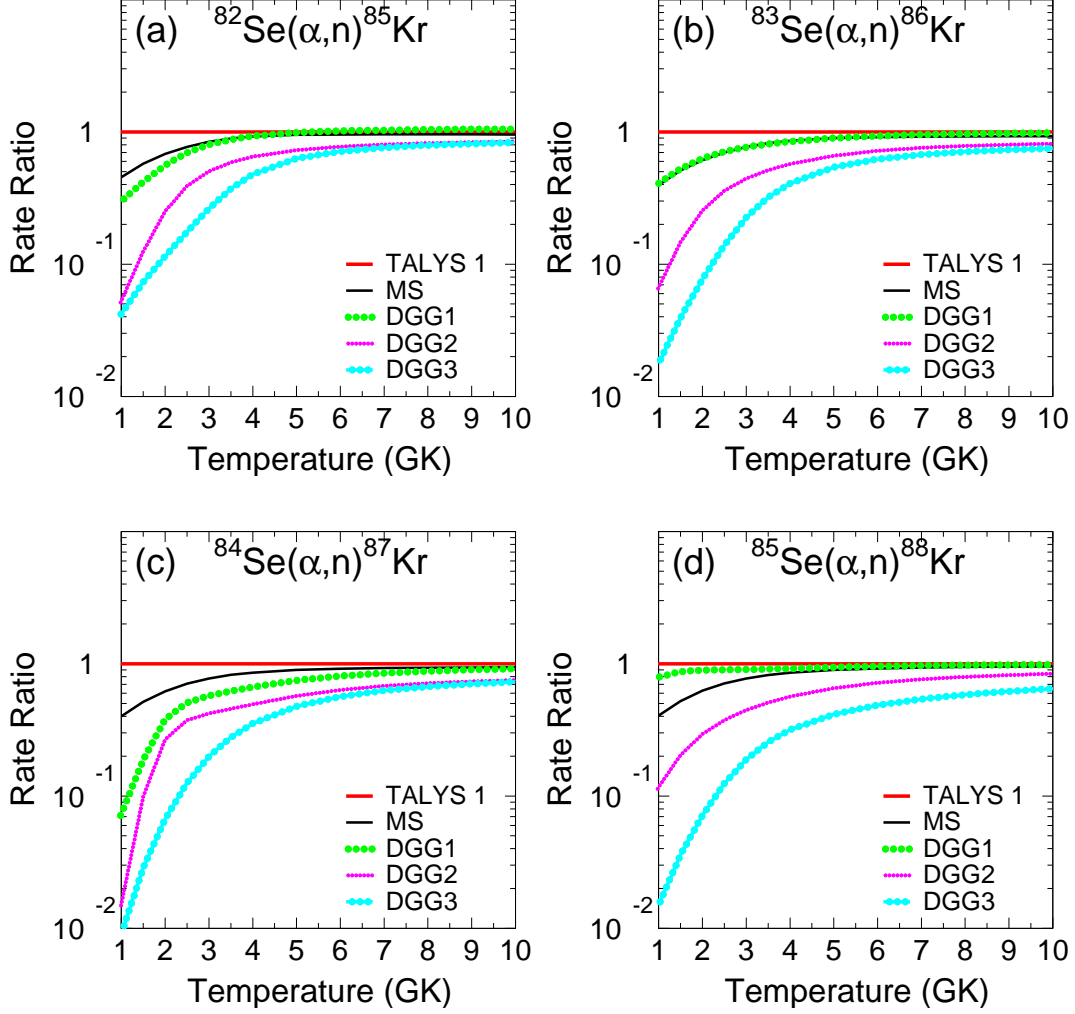


FIG. 7: (Color online) TALYS rates for the reactions (a) $^{82}\text{Se}(\alpha, n)^{85}\text{Kr}$; (b) $^{83}\text{Se}(\alpha, n)^{86}\text{Kr}$; (c) $^{84}\text{Se}(\alpha, n)^{87}\text{Kr}$; and (d) $^{85}\text{Se}(\alpha, n)^{88}\text{Kr}$. The different lines shown in each figure were obtained using the list of AOP models listed in Table I and the packet TALYS 1 for the rest of the nuclear inputs. All the rates are normalized to the values obtained using the packet TALYS 1 for all the nuclear inputs. (See text for details.)

found that the excitation-energy logarithmic-binning algorithm used in TALYS leads to rates that are approximately one order of magnitude lower than the results obtained with the standard equidistant binning used in NON-SMOKER and in previous versions of TALYS. In addition, we also noticed that the rates published in the NON-SMOKER database correspond to the inclusive (α, n) reaction instead of the exclusive $(\alpha, 1n)$ channel which is considered in network calculations. Whereas this aspect is not important for light systems or low energies, it becomes critical when the reaction energy is comparable to the Q-values of the multiple-neutron channels. Such was the case with the reaction $^{86}\text{Se}(\alpha, n)$. This effect was also observed in other reactions like $^{74}\text{Ga}(\alpha, n)$. The impact of this inconsistency onto network-calculated abundances needs to be properly analyzed, although we

speculate that it might have a moderate impact in the α process, since (α, n) reactions are in NSE with their inverse for temperatures above $T \simeq 4$ GK.

In the second part of the paper we focused on the impact of the nuclear-input sources on the theoretical uncertainty. We compared the rates obtained with TALYS for $^{86}\text{Se}(\alpha, n)^{89}\text{Kr}$, using different sources (models or databases) to determine alpha optical potentials, masses, level densities, proton/neutron optical potentials, pre-equilibrium, level structure, radiative transmission coefficients, and width fluctuation correction factors. Clearly, the most important nuclear input for α -process reactions is the alpha optical potential. The use of different alpha optical potential models led to differences in the calculated rates of up to two orders of magnitude at temperatures $T \lesssim 4$ GK. These differences were seen for other re-

actions: $^{82}\text{Se}(\alpha, n)^{85}\text{Kr}$, $^{83}\text{Se}(\alpha, n)^{86}\text{Kr}$, $^{84}\text{Se}(\alpha, n)^{87}\text{Kr}$, and $^{85}\text{Se}(\alpha, n)^{88}\text{Kr}$. As for the other nuclear inputs, the theoretical uncertainty arising from the use of different sources was only significant at high temperatures. In particular, the maximum deviations in the calculate rates due to these nuclear inputs were: a factor 2 for nuclear masses, a factor 10 for level densities, and 50% for proton/neutron optical potentials and preequilibrium. On the other hand, the sensitivity of the calculated rates to the models used to determine the radiative transmission coefficient and the width fluctuation correction was negligible.

The results obtained in this work underline the necessity of measuring the (α, n) reactions (inclusive and exclusive channels) involved in the nucleosynthesis of the α process. Of crucial importance are the measurements of alpha optical potentials in regions where direct studies of the reactions are not possible experimentally.

Finally, in a forthcoming paper we will present a discussion of the most important (α, n) reactions for the nucleosynthesis of light r-process nuclei in the α process at different astrophysical conditions, and the impact of their theoretical uncertainty on the calculated abundances.

Appendix: NUCLEAR INPUTS IN TALYS AND NON-SMOKER

The reaction rates calculated by codes like TALYS and NON-SMOKER depend on some important nuclear properties (nuclear inputs). In this section, we briefly summarize the models and options provided by TALYS and NON-SMOKER to calculate the most important inputs. Each of these models are listed in Table I of Sec. III A.

1. Optical potential

In the present work, we have used five of the proton/neutron optical potential models included in TALYS, namely the global optical model (GOP), and the Bauge-Delaroche-Girod model (BDG0), with three possible additional variations (BDG1–3). In addition, NON-SMOKER uses the Jeukenne-Lejeunne-Mahaux model (JLM).

Following the notation of Ref. [1], the optical model potential (OP) is defined as:

$$U(r, E) = V(r, E) + iW(r, E) + V_c(r, E), \quad (\text{A.1})$$

where $V(r, E)$ is the real part, $W(r, E)$ is the imaginary part, and $V_c(r, E)$ is the Coulomb potential corresponding to a uniform charged sphere of reduced radius $R_c = r_c A^{1/3}$. The real term is decomposed into volume-central $V_v(r, E)$ and spin-orbit $V_{so}(r, E)$ potentials:

$$V_v(r, E) = -\frac{V_v(E)}{1 + \exp[(r - R_v)/a_v]}, \quad (\text{A.2})$$

$$V_{so}(r, E) = -\left(\frac{\hbar}{m_\pi c}\right)^2 \frac{V_{so}(E)}{r \cdot a_{so}} \times \frac{\exp[(r - R_{so})/a_{so}]}{[1 + \exp[(r - R_{so})/a_{so}]]^2}, \quad (\text{A.3})$$

where m_π is the pion mass. The imaginary part includes volume-central $W_v(r, E)$, spin-orbit $W_{so}(r, E)$, surface-central $W_d(r, E)$ terms, given by:

$$W_v(r, E) = -\frac{W_v(E)}{1 + \exp(r - R_v)/a_v}, \quad (\text{A.4})$$

$$W_{so}(r, E) = -\left(\frac{\hbar}{m_\pi c}\right)^2 \frac{W_{so}(E)}{r \cdot a_{so}} \times \frac{\exp(r - R_{so})/a_{so}}{[1 + \exp(r - R_{so})/a_{so}]^2}, \quad (\text{A.5})$$

and

$$W_d(r, E) = 4W_d(E) \frac{\exp(r - R_d)/a_d}{[1 + \exp(r - R_d)/a_d]^2}. \quad (\text{A.6})$$

In some cases, it is possible to take the parameters in these equations from local fits to specific nuclei.

a. Global optical model potential (GOP)

In the present work, we have used the TALYS global optical potential (GOP) [1] in the default packet TALYS 1 (see Table II). In this model, r_v , a_v , r_d , a_d , r_{so} , a_{so} , r_c are constant, and $V_v(E)$, $W_v(E)$, $W_d(E)$, $V_{so}(E)$, and $W_{so}(E)$ are functions which depend on the particle projectile energy in the laboratory frame E and the Fermi energy E_F (determined by the chosen mass model). The value of the parameters used in these function, validated for $0.001 \leq E \leq 200 \text{ MeV}$ and $24 \leq A \leq 209$, are reported in Eqs. 4.8 and 4.9, and Tables 4.1 and 4.2 of Ref. [1] for neutrons and protons, respectively.

b. Jeukenne-Lejeunne-Mahaux model (JLM)

As described in Ref. [38], NON-SMOKER uses the semi-microscopic optical potential of Jeukenne-Lejeunne-Mahaux [40] (JLM). In a first step, these authors followed the Brueckner-Hartree-Fock approximation [59, 60] to calculate the isoscalar, isovector, and Coulomb components of the OP of infinite nuclear matter (INM) using the Reid's hard-core nucleon-nucleon potential [61]. The numerical results were then parameterized in terms of density and energy $U_{INM}(\rho, E)$ for energies up to 160 MeV. The finite-nuclear-matter (FNM) OP was then constructed using the local-density-approximation (LDA) $U_{FNM}(r, E) \simeq U_{INM}(\rho(r), E)$, where r is the

distance from the nuclear center. This LDA, can be improved (ILDA) by introducing a Gaussian form factor. The NON-SMOKER OP includes the corrections of the imaginary part described in [41, 42].

Since there is not enough details provided in Ref [38] to implement this model in TALYS, we decided to use the BDG0 model (described below) in the packet TALYS 2 (discussed in Sec. III B) as a good approximation.

c. Bauge-Delaroche-Girod model (BDG)

TALYS includes the semi-microscopic optical model of Bauge-Delaroche-Girod [39] (BDG), which is based on the Jeukenne-Lejeunne-Mahaux potential [40]. Following the ILDA, the OP of a nucleus is calculated by folding the Bauge-Delaroche-Girod INM optical potential $U_{INM}(\rho, E)$ [39], using the radial matter density $\rho(r)$ from the nuclear structure database. The INM potential includes corrections to unify the low and high energy parameterizations of the interaction [62], and to renormalize the isovector component necessary to account simultaneously for (p, n) and (n, n) elastic scattering, and $(p, n)_{IAS}$ quasi-elastic scattering [39]. The spin-orbit potential for the finite nucleus is described in Ref. [1]. Besides the standard version of the BDG potential (BDG0), TALYS offers three possible renormalizations of the imaginary isovector coefficient, which we label BDG1, BDG2, and BDG3 [1].

2. Alpha optical potentials

In the present work, we used five different alpha optical potentials included in TALYS [1]:

a. Global alpha optical potential (GAOP)

The global alpha-optical potential (GAOP) is used in the default packet TALYS 1 (see Table II). It is formulated in terms of the neutron and proton spherical optical potentials [63]. The real term $V(r, E)$ of Eq. A.1 corresponds to a volume-central potential:

$$V(r, E) = -2 \frac{2 \sum_{i=n,p} V_v^i(E/4)}{1 + \exp[(r - R_v)/a_v]}. \quad (\text{A.7})$$

The imaginary part of Eq. A.1 is defined in terms of the volume-central $W_v(r, E)$ and surface-central $W_d(r, E)$ terms, according to:

$$W_v(r, E) = - \frac{2 \sum_{i=n,p} W_v^i(E/4)}{1 + \exp[(r - R_v)/a_v]}, \quad (\text{A.8})$$

and

$$W_d(r, E) = 4 \frac{2 \sum_{i=n,p} W_d^i(E/4) \exp[(r - R_d)/a_d]}{[1 + \exp[(r - R_d)/a_d]]^2}, \quad (\text{A.9})$$

where the functions $V_v(E)$, $W_v(E)$, $W_d(E)$, $V_{so}(E)$, and $W_{so}(E)$ are defined in Eqs. 4.8 and 4.9, and Tables 4.1 and 4.2 of Ref. [1] for neutrons and protons, respectively.

b. Alpha optical potential of McFadden and Satchler (MS)

Another possible alpha optical potential used by TALYS is based on the studies of McFadden and Satchler (MS) [29]. They used a simplified version of the optical potential that only includes a volume-central real and imaginary terms, and the Coulomb potential term with the reduced radius $r_c = 1.3 \text{ fm}$. The potential was obtained by adjusting the fit parameters to elastic scattering data of 24.7 MeV alpha particles on a large sample of nuclei. Although these authors emphasized that no satisfactory fit to all nuclei was possible, their best fit was given by $V_v = 185 \text{ MeV}$, $W_v = 25 \text{ MeV}$, $R_v = 1.4 \text{ fm}$, and $a_v = 0.52 \text{ fm}$.

As shown in Table II, the MS AOP is used in NON-SMOKER and the TALYS packet TALYS 2 introduced in Sec. III B.

c. Alpha optical potential of Demetriou-Grama-Goriely (DGG)

In the DGG potential [30], the Coulomb term $V_c(r, E)$ corresponds to a uniform charged sphere with a reduced radius $r_c = 1.25 \text{ fm}$. The real term $V(r, E)$ is given by:

$$V(r, E) = \lambda V_{DF}(r, E), \quad (\text{A.10})$$

where λ is a strength parameter, and $V_{DF}(r, E)$ is the potential calculated using the double-folding model of Kobos *et al.* [64]. The imaginary part of the DGG potential is described by a Wood-Saxon function. TALYS includes three different formulations of $W(r, E)$. The first choice DGG1 includes a central-volume term only, with geometrical parameters given by Eq. 17 and Table I of Ref. [30], and an energy dependency described by Eqs. 22–24 and Table I of Ref. [30]. The second possible alpha potential DGG2 corresponds to DGG1 with geometrical parameters given by Eq. 20 and Table II of Ref. [30], and a surface term with the same energy dependency than the volume term and derived from the same Wood-Saxon function, but 90% of its depth. Finally, the third potential DGG3 corresponds to DGG2 with a damping function for the surface term to account for the known decrease of the surface absorption with increasing energies, as described in Ref. [30].

3. Masses

In the present work, we have used three theoretical mass models: the macroscopic-microscopic finite-range droplet model of Möller *et al.* (FRDM) [31] (which is

the model used in NON-SMOKER), and the HFB mass tables of Goriely *et al.* with a Skyrme-type (SHFB) [32] or Gogny-type (GHFB) [33] forces. In addition, we also used the experimental Audi Wapstra mass table (Audi 2003) [28] included in TALYS.

a. Skyrme-Hartree-Fock-Bogoliubov nuclear mass model (SHFB)

The SHFB mass model is the option included in the packet TALYS 1 (see Table II). It is based on the HFB method, using a 10-parameter Skyrme force and the contact pairing force described in Ref. [32]. The pairing gaps are calculated microscopically for symmetric nuclear matter and neutron matter, and include medium polarization effects, as described in Ref. [65]. The calculated HFB energy includes a phenomenological Wigner term and a collective-correction term to account for the rotational and vibrational spurious energy. All the fit parameters were determined using a set of 2149 measured masses. Moreover, in order to improve the predictive power, particularly for neutron-rich nuclei, while minimizing the rms error of the fit, several conditions were imposed during the fitting process. First, the model was requested to reproduce the energy per nucleon of pure infinite neutron matter for all densities up to the value for nuclear matter. For that purpose, the microscopically calculated equation of state (including two- and three-nucleon forces) of Friedman and Pandharipande [66] was used as reference. Second, the contact pairing force was constrained to reproduce exactly the density dependence of the 1S_0 pairing gap of neutron matter calculated by Cao *et al.* [65], using the Argonne force v_{18} [67] and the three-body force of Grangé *et al.* [68]. The resulting fit parameters are listed in Table I of Ref. [32]. The rms deviation of the SHFB masses with respect to the chosen set of 2149 measured masses was 0.581 MeV.

b. Gogny-Hartree-Fock-Bogoliubov nuclear mass formula (GHFB)

The GHFB model uses a 14-parameter Gogny force specially developed to deal with neutron-rich nuclei [33]. It includes a quadrupole-correlation correction calculated within the 5DCH model using a triaxially-deformed HFB code [69], and an infinite-basis correction to account for the limited number of shells included in the calculation. The parameters of the model were determined using the fit method described in Ref. [33], which includes the measured masses of 2149 nuclei and charge radii. As in SHFB, the fit was requested to reproduce qualitatively the energy-density curves of infinite neutron matter [66] and symmetric matter calculated by Li *et al.* [70]. The resulting set of fit parameters are given in Table I of Ref. [33]. The rms deviation of the GHFB masses with respect to the chosen set of 2149 measured masses was

0.789 MeV.

c. Finite-range droplet model (FRDM)

The third mass model used in the present work was the macroscopic-microscopic FRDM [31]. The macroscopic part of the model is divided in volume E_v , surface E_s and Coulomb terms E_c . Each of these terms are formulated as a Taylor expansion to second order on three fundamental variables related to the neutron skin thickness, the variation of the density with respect to the saturation value for symmetric matter (i.e. nuclear dilatation), and the asymmetry of nuclear matter. The resulting macroscopic energy formula depends on the shape of the nucleus and includes terms that account for pairing effects, charge asymmetry, and the Wigner energy. In addition, a pure phenomenological term is included to improve the description of compressibility effects. The values of all constants in the model are given in Ref. [31].

The FRDM model includes a shell-plus-pairing microscopic correction of the macroscopic energy based on the Strutinsky method [71]. The single-particle potential used in the shell-correction part includes folded-Yukawa, spin-orbit, and Coulomb terms. The pairing correction uses a seniority force treated in the Lipkin-Nogami method. An additional correction is added to account for spurious motion due to the zero-point energy of vibrational modes.

In order to describe nuclear shapes, FRDM adopted the Nilsson-perturbed spheroidal parameterization (or ϵ parameterization). The potential-energy surfaces were calculated in terms of ϵ_2 , ϵ_4 , ϵ_3 , and ϵ_6 using a modified version of FRLDM [72]. The Folded-Yukawa single-particle model includes only axially symmetric shapes.

Overall, FRDM has 31 parameters, 12 of which were obtained from fits to experimental data set of 1654 masses with Z and $N \geq 8$ and 28 fission-barrier heights. The remaining 19 parameters were predetermined before the mass fits using properties other than nuclear masses, such as electron and heavy-ion scattering data, and measured systematics of single-particle levels. A model error $\sigma_{mod} = 0.667$ MeV is quoted by Lunney *et al.* [73] when the full 1995 data set of 1768 masses is used in the fit. This value corresponds to a rms error σ of 0.678 MeV.

Since the FRDM is used in NON-SMOKER, we have included it in the packet TALYS 2 introduced in Sec. III B.

4. Level density

TALYS provides five different models to calculate the nuclear level density $\rho(E)$: the constant temperature model (CTM), the Back-Shifted Fermi gas model (BFM), the generalized superfluidity model (GSM), and the statistical microscopic model (SCM) and combinatorial microscopic model (CMM). In addition, we have

also coded and included the Rauscher-Thieleman-Kratz level-density model (RTK) used in NON-SMOKER [38].

This sections gives a brief summary of their main features. A detailed description can be found in Ref. [74].

a. Constant temperature model (CTM)

In the CTM model [34], the level density is described by the Fermi gas model, according to:

$$\rho_{FG}(E) = \frac{1}{\sqrt{2\pi\sigma}} \frac{e^S}{\sqrt{D}}, \quad (\text{A.11})$$

where $D = \sqrt{12/\pi} a U^{5/2}$; $S = 2\sqrt{aU}$; σ^2 is the so-called spin cut-off parameter; and U is the excitation energy corrected by the pairing energy gap Δ according to $U = E - \Delta$, where $\Delta = 12\chi/\sqrt{A}$, and $\chi=0,1$ or 2 for odd-odd, odd-even or even-even numbers of proton and neutron, respectively. The shell-corrected level-density parameter a includes the damping of shell effects with energy:

$$a(E) = \tilde{a} \left(1 + \delta W \frac{1 - e^{-\gamma U}}{U} \right), \quad (\text{A.12})$$

where $\tilde{a} = \alpha A + \beta A^{2/3}$ is the asymptotic ($E \rightarrow \infty$) level density in the absence of shell effects; $\gamma = \gamma_1/\sqrt{A} + \gamma_2$ is the damping parameter; and δW is the difference between the experimental mass of the nucleus and its value calculated with the spherical liquid-drop model [75]. The parameters α , β , γ_1 and γ_2 were determined to describe the average level density over a whole range of nuclei; their default values are reported in Table 4.3 of Ref. [1]. As for the spin cut-off parameter, TALYS uses the expression:

$$\sigma^2 = \frac{I_0}{\hbar^2} \frac{a}{\tilde{a}} \sqrt{\frac{U}{a}}, \quad (\text{A.13})$$

with the moment of inertia of the undeformed nucleus of radius R given by:

$$I_0 = \frac{2}{5} m_0 A R^2, \quad (\text{A.14})$$

where A is the mass number, and m_0 is the neutron mass.

At low energies, the CTM assumes that the number of cumulative levels follows an exponential law:

$$\rho_{CT}(E) = \frac{1}{T} \exp \left(\frac{E - E_0}{T} \right), \quad (\text{A.15})$$

where the value of the temperature T and E_0 are used as adjusting parameters to reproduce experimental discrete levels. The values of these parameters, along with the cut-off matching energy E_M are deduced by the requirement that $\rho_{FG}(E)$ and $\rho_{CT}(E)$ must be matched at the energy E_M .

This phenomenological model, along with the BFM, GSM, and RTK explained below, can be corrected to account for the presence of collective levels due to rotational

and (to a lesser degree) vibrational modes, as explained in Sec. 4.7.2 of Ref. [1]. This correction is important in fission, where the large deformations at and beyond the saddle point favor the appearance of rotational levels. In TALYS, the collective enhancement is considered by default only when fission is included in the reaction. Therefore, in the present work, we have excluded this correction because the nuclei involved in the α process are non-fissile.

b. Back-shifted Fermi gas model (BFM)

The BFM model uses the level density of the Fermi gas model given by Eq. A.11 with the pairing energy term Δ including an adjustable energy-shift parameter δ . Moreover, the correction of the zero-energy divergence problem [76] leads to [35]:

$$\rho(E) = \left[\frac{1}{\rho_{FG}(E)} + \rho_0 \right]^{-1}, \quad (\text{A.16})$$

where ρ_0 is given by Eq. 4.281 of Ref. [1].

In the present work, the BFM did not include collective-enhancement corrections.

c. Generalized superfluid model (GSM)

In the GSM of Ignatyuk et al. [36], the level density is characterized by a superfluidity phase at low energies, and a Fermi-gas phase at higher energies. The transition point is defined by a critical energy:

$$U_c = a_c T_c^2 + E_{cond}, \quad (\text{A.17})$$

where $T_c = 0.567\Delta_0$; Δ_0 is the pairing correlation energy given by $\Delta_0 = 12/\sqrt{A}$; E_{cond} is the condensation energy expressed as $E_{cond} = (3/2\pi^2)a_c\Delta_0^2$; and a_c is the critical level-density parameter described iteratively by Eq 4.278 of Ref. [1]. At energies lower than U_c , the level density is defined by Eq. A.11, with D , S , and σ^2 given by Eqs. 4.287–4.289 of Ref. [1]. For higher energies, the model follows the Fermi gas level density with an effective excitation energy that depends on the condensation energy E_{cond} , the pairing correlation energy Δ_0 , and an adjustable energy-shift parameter.

As mentioned above, in the present work we did not include collective-enhancement corrections for this phenomenological model.

d. Microscopic models

In the present work, we have used two more level-density models included in TALYS: The statistical microscopic model (SMM) of Demetriou and Goriely [35], and the combinatorial microscopic model (CMM) [37].

(We believe that the reference number [531] given for the SMM model in Sec. 4.7.3 of Ref. [1] should actually correspond to Ref. [35] in the present paper.)

The SMM is based on the partition function method, which uses the level density given by Eqs. A.11 and A.16, where the determinant D is formulated following Moretto [77], and the entropy and excitation energy are derived by summing the doubly-degenerate single-particle levels for protons and neutrons, as described in Sec. 2 of Ref. [35]. In addition, this model includes a phenomenological prescription for the collective enhancement K due to rotations only, where the perpendicular spin cut-off parameter includes pairing correlations as given by Eq. 10 of Ref. [35]. All the microscopic quantities used in the model, namely single-particle energies, pairing-gap strength, deformation parameters and moment of inertia, are determined from the Hartree-Fock-BCS model of Goriely *et al.* [78], using the effective force MSk7.

The CMM used in the present work uses the Hatree-Fock-Bogoliubov calculation [79], based on the BSk14 effective interaction, to construct incoherent particle-hole state densities as a function of excitation energy, spin projection on the intrinsic symmetry axis K , and parity P . The collective enhancement due to rotational motion was taken into account by considering the rotational bands built from any intrinsic states of specific projection K and parity P . As for the collective vibrational enhancement factor, it is described using the boson partition function with the phonon state densities constructed and folded with the incoherent particle-hole densities.

e. Rauscher-Thielemann-Kratz model (RTK)

In NON-SMOKER, the level densities are calculated using the Rauscher-Thielemann-Kratz model [38], which is a hybrid between the CTM and the BFM described above. Since this model is not included in TALYS, we had to code it and add it to the TALYS packet TALYS 2 discussed in Sec. IIIB.

In the RTK model, the level density is calculated using the Fermi-gas expression of Eq. A.11 with some important differences:

First, the pairing-gap correction Δ is identified with the back-shifted term and calculated according to:

$$\Delta = \frac{1}{2} [2B(Z, N) - B(Z, N - 1) - B(Z, N + 1)] \quad (\text{A.18})$$

for neutrons, and

$$\Delta = \frac{1}{2} [2B(Z, N) - B(Z - 1, N) - B(Z + 1, N)] \quad (\text{A.19})$$

for protons; where $B(Z, N)$ is the binding energy for the nucleus (Z, N) . We calculated Δ for each nuclei involved in the reaction, using the experimental Audi Wapstra mass table (Audi 2003) [28] for the binding energies.

Second, the spin cut-off parameter given by Eq. A.20 is replaced by:

$$\sigma^2 = \frac{I_0}{\hbar^2} \sqrt{\frac{U}{a}}, \quad (\text{A.20})$$

Third, the coefficients α and β , used to calculate \tilde{a} in Eq. A.12, and the shell-effect dumping parameter γ , were determined in [38] from fits to measured s-wave neutron resonance spacing of 272 nuclei at the neutron separation energy. We used the resulting values $\alpha=0.1337$, $\beta=-0.06571$, and $\gamma=0.04884$ [38].

Fourth, the shell-correction term δW of Eq. A.12, is identified with the so-called microscopic correction E_{mic} . Following the discussion of Ref. [38], we took the values of E_{mic} from [31] for the nuclei involved in the reaction.

Fifth, in the RTK model described in [38], the divergence of the level density at low energies ($U \sim \Delta$) is avoided by matching ρ_{FG} to

$$\rho(U) \propto \frac{\exp(U/T)}{T} \quad (\text{A.21})$$

using a tangential-fit method [34, 80] to determine T . However, in the present work we followed the matching method used in TALYS described above for the CTM.

Finally, like with the other phenomenological models included in TALYS, the collective enhancement of the level density was not included for this model.

5. Pre-equilibrium

For a given reaction, TALYS considers three possible reaction mechanisms, namely direct, compound and pre-equilibrium, which is described using the EXCITON model [27]. Their distinction is usually described in terms of the number of intranuclear binary collisions involved in the reactions: one or two for direct reactions, few for pre-equilibrium, and many for compound-nucleus reactions. Their importance depends largely on the energy of the projectile particle and, on a lesser degree, the mass of the target nucleus (see Ref. [1] for more details). It is important to clarify that these three components are not decoupled. In one hand, the pre-equilibrium formalism includes by definition the direct component to the continuum. On the other hand, after the pre-equilibrium stage, the reaction sequence might still continue with the incident particle interacting with an increasing number of nucleons until statistical equilibrium is attained, i.e. leading to a compound-nucleus reaction. Thus, disabling the calculation of the pre-equilibrium mechanism will affect the contributions from the compound and direct components.

The EXCITON model is formulated in terms of internal transition rates (λ_π^+ , λ_ν^+ , $\lambda_{\pi\nu}^0$, $\lambda_{\nu\pi}^0$) which describe the creation of proton (neutron) particle-hole pairs λ_π^+ (λ_ν^+), and the conversion between proton and neutron particle-hole pairs $\lambda_{\pi\nu}^0$ and $\lambda_{\nu\pi}^0$. These quantities depend on the

proton-proton, neutron-neutron, and proton-neutron collision probabilities. In the present work, we have used three different methods included in TALYS to calculate these collision probabilities. The first two methods (labeled PREEQ1 and PREEQ2) use an effective squared matrix element to represent the effective residual interaction. The resulting transition rates can be solved analytically (PREEQ1) or numerically (PREEQ2). The third method (PREEQ3) calculates the collision probabilities using the imaginary optical potential depth instead of the effective squared matrix element. TALYS includes a fourth option (PREEQ4) which assumes that pre-equilibrium occurs only for the first binary collision. In that case, the subsequent population of discrete and continuum levels is considered using the multi-step Hauser-Feshbach decay formalism. In the present work, we have used the TALYS default option PREEQ2 in the packet TALYS 1 and disabled preequilibrium in the packet TALYS 2 (see Table II).

6. Level structure

By default, TALYS takes the experimentally-known discrete level information (energy, spin, parity, etc.) from the Reference Input Parameter Library (RIPL-3) [43], and uses theoretical level densities to extend the level sequence to at least 100 levels. This option (labeled RIPL+th) was used in the default packet TALYS 1, as shown in Table II. On the other hand, NON-SMOKER uses up to 19 experimentally known discrete levels, taken from Firestone's Table of Isotopes [44]. Likewise, the TALYS packet TALYS 2 described in Sec. IIIB uses only up to 19 experimental levels from RIPL-3 [43] (label RIPL in Table II).

As for the nuclear deformation, TALYS and NON-SMOKER use their mass models to calculate the ground-state deformation. Thus, in the default packet TALYS 1, the ground-state deformations are calculated from SHFB, whereas TALYS 2 and NON-SMOKER use FRDM.

7. Radiative transmission coefficients

The radiative (or gamma-ray) transmission coefficient for X -type radiation (E or M) of ℓ multipolarity is given by:

$$T_{\gamma,X\ell}(E_\gamma) = 2\pi f_{X\ell} E_\gamma^{2\ell+1}, \quad (\text{A.22})$$

where E_γ is the gamma energy and $f_{X\ell}$ is the radiative strength function. For transitions other than $E1$, TALYS calculates $f_{X\ell}$ using the Brink-Axel Lorentzian formula [45] (see Eq. 4.67 of [1]), with the giant resonance strengths $\sigma_{X\ell}$, energies $E_{X\ell}$, and widths $\Gamma_{X\ell}$ taken from the formulae by Kopecky [43] (Eqs. 4.73–4.76 of [1]). For $E1$ transition, TALYS includes five possible formulations of $f_{X\ell}$:

1. Brink-Axel formula (BA) [45],
2. Kopecky-Uhl formula (KU) [46] (used in TALYS 1, Table II),
3. Hartree-Fock BCS tables (HF-BCS) [1],
4. Hartree-Fock-Bogolyubov tables (HFB) [1],
5. Goriely's hybrid model (GH) [47],

where the strengths, energies, and widths of the GDR are taken from measured data (RIPL-3), if available, or from Kopecky's formulae [43].

In the present work, we have calculated $T_{\gamma,X\ell}$ using the five different formulations of the strength function listed above for $E1$, and the Brink-Axel Lorentzian for $M1$, $E2$, and $M2$.

Apart from the options originally included in TALYS, we have also coded the Cowan-Thielemann-Truran (CTT) formulation [38, 48] of the radiative transmission coefficients used by NON-SMOKER. In this case, only $E1$ and $M1$ transitions were included. For $T_{\gamma,M1}$, we followed the formulation by Blatt and Weisskopf (see Eq. 17 of [81]), whereas $T_{\gamma,E1}$ was calculated using the Lorentzian representation of the GDR given by Eq. 7 of [38]. The GDR parameters were calculated following Myers *et al.* [82] for energies, and Thielemann-Amould [83] for widths. For the later, we also included the energy-dependent correction described by McCullagh *et al.* [84] (Eq. 6 of [56]), which is important for low-energy gamma transitions. The new coded subroutine was used in the TALYS 2 packet (see Table II).

8. Width fluctuation correction

At low energies, the compound-nucleus cross section needs to be corrected to account for the correlation between incident and outgoing waves. This is done by including the so-called width fluctuation correction (WFC) factor. In the present work, we have used the three formulations of the WFC included in TALYS [1]:

1. Hofmann-Richert-Tepel-Weidenmüller (HRTW1) model [49],
2. Moldauer [52] model (used in TALYS 1, Table II),
3. Gaussian orthogonal ensemble (GOE) of Hamiltonian matrices [53].

Although NON-SMOKER calculates the WFC factor using the Hofmann-Richert-Tepel-Weidenmüller model [49], the expression of enhancement factor W_j (following the notation used in [56]) given by Tepel *et al.* [50] (see Eq. 5 of [56]) differs from the formulation used by TALYS [51]. In the present work, we coded the NON-SMOKER HRTW model (HRTW2) to define the packet TALYS 2 (see Table II).

Acknowledgments

The authors want to express their gratitude to Dr. A. Arcones for fruitful discussions during the preparation of the present paper. Constructive comments from

the anonymous referee are highly appreciated.

This work was supported by the America National Science Foundation grants PHY 08-22648 (JINA), PHY 01-10253.

-
- [1] A. J. Koning, S. Hilaire, and S. Gorieli, *Talys 1.6 user manual* (2013), URL <http://www.talys.eu/fileadmin/talys/user/docs/talys1.6.pdf>.
 - [2] T. Rauscher, *Non-smoker code*, URL <http://nucastro.org/nonsmoker.html>.
 - [3] R. Crowter, *PhD. dissertation* (University of Surrey, 2007).
 - [4] F. Käppeler, R. Gallino, S. Bisterzo, and W. Aoki, *Rev. Mod. Phys.* **83**, 157 (2011).
 - [5] M. Arnould and S. Goriely, *Phys. Rep.* **384**, 1 (2003).
 - [6] S. E. Woosley, D. H. Hartmann, R. D. Hoffman, and W. C. Haxton, *Astrophys. J* **356**, 272 (1990).
 - [7] C. Fröhlich, G. Martínez-Pinedo, M. Liebedörfer, F.-K. Thielemann, E. Bravo, W. R. Hix, K. Langanke, and N. T. Zinner, *Phys. Rev. Lett.* **96**, 142502 (2006).
 - [8] J. J. Cowan and W. K. Rose, *Astrophys. J* **212**, 149 (1977).
 - [9] S. E. Woosley and R. D. Hoffman, *Astrophys. J* **395**, 202 (1992).
 - [10] T. C. Beers and N. Christlieb, *Annu. Rev. Astron. Astrophys.* **43**, 531 (2005).
 - [11] C. Sneden, J. J. Cowan, and R. Gallino, *Annu. Rev. Astron. Astrophys.* **46**, 241 (2008).
 - [12] T. Rauscher, *Astrophys. Journal. Supl. Series* **201**, 16 (2012).
 - [13] M. Beard, E. Uberseder, R. Crowter, and M. Wiescher, *Phys. Rev. C* **90**, 034619 (2014).
 - [14] R. Surman, J. Beun, G. C. McLaughlin, and W. R. Hix, *Phys. Rev. C* **79**, 045809 (2009).
 - [15] J. Beun, J. C. Blackmon, W. R. Hix, G. C. McLaughlin, M. S. Smith, and R. Surman, *J. Phys. G* **36**, 025201 (2009).
 - [16] M. Mumpower, G. C. McLaughlin, and R. Surman, *Phys. Rev. C* **86**, 035803 (2012).
 - [17] M. G. Bertolli, F. Herwig, M. Pignatari, and T. Kawano, *arXiv astro-ph* **1310.4578v1**, 1 (2013).
 - [18] J. Witt, H.-T. Janka, and K. Takahashi, *Astron. Astrophys.* **286**, 841 (1994).
 - [19] A. Simon, M. Beard, A. Spyrou, S. J. Quinn, B. Bucher, M. Couder, P. A. DeYoung, A. C. Dombos, J. Grres, A. Kontos, et al., *Phys. Rev. C* **92**, 025806 (2015).
 - [20] C. Freiburghaus, J.-F. Rembges, T. Rauscher, E. Kolbe, F.-K. Thielemann, K.-L. Kratz, B. Pfeiffer, and J. Cowan, *Astrophys. J* **516**, 38 (1999).
 - [21] Y.-Z. Qian and G. Wasserburg, *Phys. Rep.* **442**, 237 (2007).
 - [22] Y.-Z. Qian and G. Wasserburg, *Astrophys. J* **687**, 272 (2008).
 - [23] A. Arcones and F. Montes, *Astrophys. J* **731**, 11 (2001).
 - [24] W. Hauser and H. Feshbach, *Phys. Rev.* **87**, 366 (1952).
 - [25] G. R. Satchler, *Nucl. Phys.* **55**, 1 (1964).
 - [26] T. Tamura, *Rev. Mod. Phys.* **37**, 864 (1965).
 - [27] A. J. Koning and J. P. Delaroche, *Nucl. Phys. A* **713**, 231 (2003).
 - [28] G. Audi and A. H. Wapstra, *Nucl. Phys. A* **729**, 129 (2003).
 - [29] L. McFadden and G. R. Satchler, *Nucl. Phys.* **84**, 177 (1966).
 - [30] P. Demetriou, C. Grama, and S. Goriely, *Nucl. Phys. A* **707**, 253 (2002).
 - [31] P. Möller, J. R. Nix, W. D. Myers, and W. J. Swiatecki, *At. Data and Nucl. Data Tables* **59**, 185 (1995).
 - [32] S. Gorieli, N. Chamel, and J. Pearson, *Phys. Rev. Lett.* **102**, 152503 (2009).
 - [33] S. Gorieli, S. Hilaire, M. Girod, and S. Perú, *Phys. Rev. Lett.* **102**, 242501 (2009).
 - [34] A. Gilbert and A. G. W. Cameron, *Can. J. Phys.* **43**, 1446 (1965).
 - [35] P. Demetriou and S. Goriely, *Nucl. Phys. A* **695**, 95 (2001).
 - [36] A. V. Ignatyuk, J. L. Weil, S. Raman, and S. Kahane, *Phys. Rev. C* **47**, 1507 (1993).
 - [37] S. Gorieli, S. Hilaire, and A. J. Koning, *Phys. Rev. C* **78**, 064307 (2008).
 - [38] T. Raucher, F.-L. Thielemann, and K.-L. Kratz, *Phys. Rev. C* **56**, 1613 (1997).
 - [39] E. Bauge, J. P. Delaroche, and M. Girod, *Phys. Rev. C* **63**, 024607 (2001).
 - [40] J. P. Jeukenne, A. Lejeunne, and C. Mahaux, *Phys. Rev. C* **16**, 80 (1977).
 - [41] S. Fantoni, B. Friman, and C. Mahaux, *Phys. Rev. Lett.* **48**, 1089 (1981).
 - [42] C. Mahaux, *Phys. Rev. C* **82**, 1848 (1982).
 - [43] R. Capote, M. Herman, P. Oblozinsky, P. G. Young, S. Goriely, T. Belgia, A. V. Ignatyuk, A. J. Koning, S. Hilaire, V. Plujko, et al., *Nucl. Data Sheets* **110**, 3107 (2009).
 - [44] R. B. Firestone, *Table of Isotopes* (Wiley, New York, 1996), 8th ed.
 - [45] D. M. Brink, *Nucl. Phys.* **4**, 215 (1957).
 - [46] J. Kopecky and M. Uhl, *Phys. Rev. C* **41**, 1941 (1990).
 - [47] S. Goriely, *Phys. Lett. B* **436**, 10 (1998).
 - [48] J. J. Cowan, F.-K. Thielemann, and J. W. Truran, *Phys. Rep.* **208**, 267 (1991).
 - [49] H. M. Hoffman, J. Richert, J. W. Tepel, and H. A. Weidenmüller, *Ann. Phys. (NY)* **90**, 403 (1975).
 - [50] J. W. Tepel, H. M. Hoffman, and H. A. Weidenmüller, *Phys. Lett. B* **49**, 1 (1974).
 - [51] H. M. Hoffman, T. Mertelmeier, M. Herman, and J. W. Tepel, *Z. Phys. A* **297**, 153 (1980).
 - [52] P. A. Moldauer, *Phys. Rev. C* **14**, 764 (1976).
 - [53] J. J. M. Verbaarschot, H. A. Weidenmüller, and M. R. Zirnbauer, *Phys. Rep.* **129**, 367 (1985).
 - [54] C. Angulo, M. Arnould, M. Rayet, P. Descouvemont, D. Baye, C. Leclercq-Willain, A. Coc, S. Barhoumi, P. Aguer, C. Rolfs, et al., *Nucl. Phys. A* **656**, 3 (1999).
 - [55] A. Scott, A. Morton, C. Tingwell, S. Tims, V. Hansper, and D. Sargood, *Nucl. Phys. A* **523**, 373 (1991).

- [56] T. Raucher and F.-L. Thielemann, *At. Data and Nucl. Data Tables* **75**, 1 (2000).
- [57] J. Bliss, A. Arcones, F. Montes, and J. Pereira, *to be submitted to Phys. Rev. C* (2016).
- [58] A. J. Koning, S. Hilaire, and S. Gorieli, *Talys 1.4 user manual* (2011), URL <http://www.talys.eu/fileadmin/talys/user/docs/talys1.4.pdf>.
- [59] J. P. Jeukenne, A. Lejeune, and C. Mahaux, *Phys. Rep.* **25**, 83 (1976).
- [60] J. P. Jeukenne, A. Lejeune, and C. Mahaux, *Phys. Rev. C* **15**, 10 (1977).
- [61] R. V. Reid, *Ann. Phys. (NY)* **50**, 411 (1968).
- [62] E. Bauge, J. P. Delaroche, and M. Girod, *Phys. Rev. C* **58**, 1118 (1998).
- [63] S. Watanabe, *Nucl. Phys. A* **8**, 484 (1958).
- [64] A. M. Kobos, B. A. Brown, R. Lindsay, and G. R. Satchler, *Nucl. Phys. A* **425**, 205 (1984).
- [65] L. G. Cao, U. Lombardo, and P. Schuck, *Phys. Rev. C* **74**, 064301 (2006).
- [66] B. Friedman and V. R. Pandharipande, *Nucl. Phys. A* **361**, 502 (1981).
- [67] R. B. Wiringa, V. G. J. Stoks, and R. Schiavilla, *Phys. Rev. C* **51**, 38 (1995).
- [68] P. Grangé, A. Lejeune, M. Martzolff, and J.-F. Mathiot, *Phys. Rev. C* **40**, 1040 (1989).
- [69] J. Libert, M. Girod, and J.-P. Delaroche, *Phys. Rev. C* **60**, 054301 (1999).
- [70] Z. H. Li, U. Lombardo, H.-J. Schulze, and W. Zuo, *Phys. Rev. C* **77**, 034316 (2008).
- [71] V. M. Strutinsky, *Nucl. Phys. A* **122**, 1 (1968).
- [72] P. Möller and J. R. Nix, *At. Data and Nucl. Data Tables* **39**, 213 (1988).
- [73] D. Lunney, J. M. Pearson, and C. Thibaut, *Rev. Mod. Phys.* **75**, 1021 (2003).
- [74] A. J. Koning, S. Hilaire, and S. Gorieli, *Nucl. Phys. A* **810**, 13 (2008).
- [75] W. D. Myers and W. J. Swiatecki, *Nucl. Phys. A* **81**, 1 (1966).
- [76] M. K. Grossjean and H. Feldmeier, *Nucl. Phys. A* **444**, 113 (1985).
- [77] L. Moretto, *Nucl. Phys. A* **185**, 145 (1972).
- [78] S. Gorieli, F. Tondeur, and J. M. Pearson, *At. Data and Nucl. Data Tables* **77**, 311 (2001).
- [79] S. Gorieli, M. Samyn, and J. M. Pearson, *Phys. Rev. C* **75**, 064312 (2007).
- [80] E. Gadioli and P. Hodgson, *Pre-equilibrium Nuclear Reactions* (Oxford Science Publications, 1992).
- [81] J. A. Holmes, S. E. Woosley, W. A. Fowler, and B. A. Zimmerman, *At. Data and Nucl. Data Tables* **18**, 305 (1976).
- [82] W. D. Myers, W. J. Swiatecki, T. Kodama, L. J. El-Jaick, and E. R. Hilf, *Phys. Rev. C* **15**, 2032 (1977).
- [83] F.-K. Thielemann and M. Arnould, in *Proc. Int. Conf. on Nuclear Data for Science and Technology* (Reidel, Dordrecht, 1983), p. 762, ed. K. Böckhoff.
- [84] C. M. McCullagh, M. L. Stelts, and R. E. Chrien, *Phys. Rev. C* **23**, 1394 (1981).